9

Personalized Anatomical Meshing of the Human Body with Applications

Yuri Vassilevski, Alexander Danilov, Yuri Ivanov, Sergey Simakov and Timur Gamilov

Abstract The frontier research in computational modeling of human physiology and medical applications is tightly connected to computational meshing technique. Meshes of hard and soft tissues, organs and network-like structures such as vessels network, trachea-bronchial tree and similar ones provide the basis for lots of simulations. We present two applications and associated numerical models requiring personalized anatomically correct meshing of the whole human body or its vascular network.

9.1 Introduction

The frontier research in computational modeling of human physiology and medical applications is tightly connected to computational meshing technique. Meshes of hard and soft tissues, organs and network-like structures such as vessels network, trachea-bronchial tree and similar ones provide the basis for lots of simulations. They are closely related to a modern virtual physiological human concept [14]. Accuracy of geometric models plays important role in every biomechanical simulation. One of the two anatomical data types is commonly assumed: general data from human

Y. Vassilevski (✉) · A. Danilov

Institute of Numerical Mathematics of Russian Academy of Sciences, 119333, Gubkina St. 8, Moscow, Russia, and Moscow Institute of Physics and Technology, 141707, Institutskii Lane 9, Dolgoprudny, Russia

e-mail: yuri.vassilevski@gmail.com; a.a.danilov@gmail.com

Y. Ivanov

Institute of Numerical Mathematics of Russian Academy of Sciences, 119333, Gubkina St. 8, Moscow, Russia

e-mail: yura-vtm@ya.ru

S. Simakov · T. Gamilov

Moscow Institute of Physics and Technology, 141707, Institutskii Lane 9, Dolgoprudny, Russia

e-mail: simakov@crec.mipt.ru; gamilov@crec.mipt.ru

anatomy atlases or individual data of the particular organism. Both data types require technical work on correct volume extraction, meshing, network skeletonisation etc.

In this paper we present two applications and associated numerical models requiring personalized anatomically correct meshing of the whole human body or its subsystems.

The first application, numerical simulation of bioelectrical impedance analysis (BIA) [5–7, 29, 44], requests a 3D meshing technique for hard and soft tissues and organs of the patient. BIA is generally used for body composition and abdominal adiposity assessment in clinical medicine, dietology, and sports medicine [12]. It is also used for body fluids redistribution monitoring under various physiological conditions.

Many factors affect correct BIA. The measured signal highly depends on electrode position, electric frequency, body constitution and shape. Accurate modeling of these processes requires adaptive geometric models either individual or the set of generic models adapted to sex, age, and important morphometry parameters (height, weight, etc). Computational analysis of the measurement schemes is the essential part of accurate data interpretation and optimization of electrode positions. Our approach is based on the direct simulation of electric current propagation through tissues and organs during bioimpedance measurements of a body segment. In this work we suggest a multi-stage algorithm to produce a personalized anatomically correct 3D mesh of the patient body. The first preliminary stage is performed once for all simulations: we use Visible Human Project data [40] as input for generation of a reference segmented model similar to [13]. At the next stages, on the basis of individual imaging data from CT/MRI we design the piecewise affine transformation of the reference body to the patient body, in order to produce its segmented geometric model. Finally, we generate the adapted tetrahedral mesh on the basis of the personalized segmented model.

The second application, network blood flow simulation [1, 10, 18, 19, 24, 30] requires a correct structural scheme (a vascular graph with nodes connected by edges) of the 3D individual vascular network. Given a 3D vascular domain extracted from CT/MRI data, one needs an algorithm producing the vascular graph. Two state-of-the-art software libraries provide tools for such functionality, commercial code Amira® [42] and open source code VMTK [41]. We use VMTK for 3D volume extraction from individual CT/MRI data for the vascular centerlines reconstruction. The vascular graph is produced from the set of centerlines by a new algorithm presented in detail in [26]. As a practical example of the personalized hemodynamic model we present simulations of revascularization procedure for the case of thigh artery stenting caused by atherosclerotic occlusion.

The proposed approach is described bellow. In Sect. 9.2 we introduce two examples of models which demand personalized anatomical meshing. In Sect. 9.3 we present our approach to anatomical meshing of patient body. In Sect. 9.4 we describe our methodology for automated generation of vascular graphs on the basis of patient CT/MRI data.

9.2 Examples of Mathematical Models Requiring Personalized Anatomical Meshing

Bioelectrical Impedance Analysis (BIA) numerical simulations require anatomically correct 3D geometrical model of the body including internal structure of organs and tissues with different electrical properties. As stated in [6], the electrical fields generated during bioimpedance measurements are governed by the equation

$$\text{div}(\mathbf{C}\nabla U) = 0 \quad \text{in} \quad \Omega \tag{9.1}$$

with the boundary conditions

$$(\mathbf{J}, \mathbf{n}) = \pm I_0/S_{\pm} \quad \text{on} \quad \Gamma_{\pm} \tag{9.2}$$

$$(\mathbf{J}, \mathbf{n}) = 0 \quad \text{on} \quad \partial\Omega \backslash \Gamma_{\pm} \tag{9.3}$$

$$U(x_0, y_0, z_0) = 0 \tag{9.4}$$

$$\mathbf{J} = \mathbf{C}\nabla U \tag{9.5}$$

where Ω is the computational domain, $\partial\Omega$ is its boundary, $\Gamma_{\pm}$ are the electrode contact surfaces, $\mathbf{n}$ is the external unit normal vector, U is the complex-valued electric potential, $\mathbf{C}$ is the complex-valued conductivity tensor, $\mathbf{J}$ is the current density, I_0 is the electric current, $S_{\pm}$ are areas of the electrode contacts. Equation (9.1) determines the distribution of electric field in the domain with heterogeneous conductivity $\mathbf{C}$. Equation (9.2) sets the constant current density on the electrode contact surfaces. Equation (9.3) defines the no-flow condition on the domain boundary. Uniqueness of the solution is guaranteed by Eq. (9.4), where (x_0, y_0, z_0) is some point in the domain Ω.

Discretization of Eqs. (9.1)–(9.5) is obtained on the basis of the conventional finite element method with the piecewise linear elements on unstructured tetrahedral meshes. We use the open source finite element and meshing library Ani3D [39]. Our approach to personalized tetrahedral meshing is presented in Sect. 9.3. Figure 9.1 represents the simulation results for the conventional four-electrode scheme with a pairs of electrodes placed on right hand and right leg.

Blood flow in the cardio-vascular network numerical simulations require anatomically correct vessel graph reconstruction. The governing equations of the hemodynamic model describe viscous incompressible fluid flow through the network of elastic tubes, see [24, 25, 30, 31] and references therein. The flow in every tube is described by mass and momentum balance as

$$\partial S_k/\partial t + \partial(S_k u_k)/\partial x = 0, \tag{9.6}$$

$$\partial u_k/\partial t + \partial\left(u_k^2/2 + p_k/\rho\right)/\partial x = f_{fr}(S_k, u_k), \tag{9.7}$$

where k is index of the tube, t is the time, x is the distance along the tube, ρ is the blood density (constant), $S_k(t, x)$ is the cross-section area, $u_k(t, x)$ is the linear velocity averaged over the cross-section, $p_k(S_k)$ is the blood pressure, f_{fr} is the
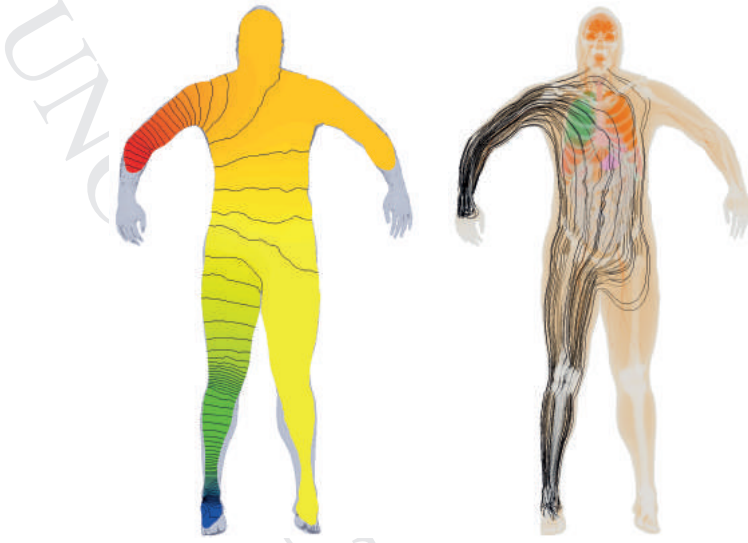
Fig. 9.1. Cutplane of the potential field (*left*) and current lines (*right*) for conventional bioimpedance measuring scheme

friction force given by

$$f_{fr}(S_k, u_k) = -\frac{4\pi\mu u_k}{S_k \tilde{S}_k}\left(\tilde{S}_k + \tilde{S}_k^{-1}\right),\tag{9.8}$$

where μ is the blood viscosity, $\tilde{S}_k = S_k/S_k^0$ and S_k^0 is the reference unstressed cross-section. At the vessels junctions the Poiseuille's pressure drop and mass conservation conditions are applied

$$p_k\left(S_k\left(t,\tilde{x}_k\right)\right) - p_{node}^l(t) = \varepsilon_k R_k^l S_k\left(t,\tilde{x}_k\right) u_k\left(t,\tilde{x}_k\right), k = k_1, k_2, \ldots, k_M,\tag{9.9}$$

$$\sum_{k=k_1,k_2,\ldots,k_M} \varepsilon_k S_k\left(t,\tilde{x}_k\right) u_k\left(t,\tilde{x}_k\right) = 0,\tag{9.10}$$

where M is the number of the connected tubes, $\{k_1,\ldots,k_M\}$ is the range of the indexes of the connected tubes, l is the node index; $p_{node}^l(t)$ is the pressure at the l-th junction point; $\varepsilon_k = 1, \tilde{x}_k = L_k$ for incoming tubes, $\varepsilon_k = -1$, and $\tilde{x}_k = 0$ for outgoing tubes, R_k^l is the hydraulic resistance. The set (9.9)–(9.10) is closed by finite differences approximation of compatibility conditions along outgoing characteristics [25]. The resulting system is reduced from $2M+1$ to M equations and is solved by Newton method separately for each junction point [24, 30]. Elasticity of the tube wall is described by the transmural pressure to cross-section relationship (wall state equation)

$$p_k(S_k) - p_{*k} = \rho c_k^2 f(S_k),\tag{9.11}$$

where S-like function $f(S)$ studied in [20] is approximated as

$$f(S_k) = \begin{cases} \exp\left(\tilde{S}_k - 1\right) - 1, & \tilde{S}_k > 1, \\ \ln \tilde{S}_k, & \tilde{S}_k \leqslant 1, \end{cases} \tag{9.12}$$

where p_{*k} is the pressure in the tissues surrounding the vessel, c_k is the pulse wave velocity (PWV) in the unstressed vessel characterizing material stiffness [35]. The relationship was verified by fiber-spring model of vessel wall elasticity [32, 33]. Equations (9.9)–(9.10) are discretized by a hybrid explicit scheme corresponding to the most accurate first order monotone scheme and the less oscillating second order scheme [15, 17].

The main geometric data for the model (9.6)–(9.12) is the vessel network in terms of 3D graph with given edge lengths, diameters and nodes positions. Our approach to personalized graph construction and meshing is presented in Sect. 9.4. In the same section we show an example of the personalized hemodynamic simulation of thigh vasculature.

9.3 Personalized 3D Meshing of the Human Body

The ideal approach for construction of anatomically correct 3D geometric model is to produce 3D geometry from individual medical images (CT, MRI or other slice-like data). This requires strong involvement of human expertise. Moreover, such data can be unavailable or have low quality due to hardware limitations, human expert qualification, medical restrictions, etc. The other reasonable approach analysed below is to fit a reference anatomically correct model. Such reference model should be based on individual data (*in vivo* [37] or detailed *post mortem* examination [40]), or a conventional database [43]. It should provide correct detailed anatomy without organs intersection and void regions due to errors in processing, segmentation, and 3D volume reconstruction algorithms. This tedious work, of course, requires human expert involvement but once the reference model is approved it could be used in automatic or semi-automatic manner.

9.3.1 Segmentation and Meshing of Reference Models

As input for the reference model we have chosen Visible Human Project (VHP) [40] data and applied a semi-automatic algorithm implemented by ITK-SNAP software [38] in order to produce a grid of labeled voxels with resolution $1 \times 1 \times 1$ mm. A detailed description of this algorithm can be found in [6].

The voxel-based geometric model of the human body is a building block to produce the unstructured tetrahedral mesh. The surface mesh can be generated by marching cubes algorithm for surface reconstruction [36], surface triangulation, smoothing and coarsening [28, 34]. The volume mesh can be generated using 3D Delaunay triangulation [9] or advancing front technique [4, 9]. We applied the Delaunay triangulation algorithm from the CGAL-Mesh library [21]. This algorithm
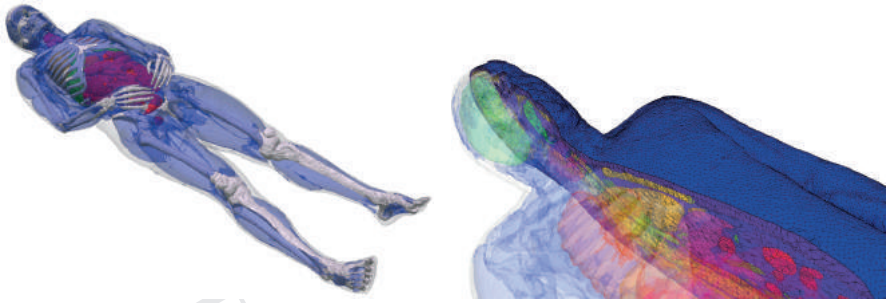
Fig. 9.2. Segmented whole body model of the Visible Human Man (*left*) and a part of related generated mesh (*right*)

allows one to use specific mesh size definition for each model material. In order to preserve geometric features of the segmented model while keeping a feasible number of vertices, we assigned smaller mesh size for the blood vessels and larger mesh size for the fat and muscle tissues. The resulted mesh contains 32 materials, 574.128 vertices and 3.300.481 tetrahedra (Fig. 9.2). This mesh retains most anatomical features of the human male body [7]. Similar model have been developed for the whole female body model.

The model was finalized by adding skin layer and multi-layered electrodes to the surface of the mesh. Boundary triangulation was used to create a prismatic mesh on the surface. Then each prism was split into three tetrahedra resulting in a conformal mesh. Mesh cosmetics algorithms from Ani3D library [39] were used to improve mesh quality. This essential step reduces discretization errors and the stiffness of the resulted system of linear equations.

9.3.2 Segmentation and Meshing of Patient-specific Models

The segmentation process is a tedious work which requires a lot of processing time. Although existing technologies of semi-automatic segmentation can speed-up the work, creating a new personalized segmented model from scratch is time consuming process. In order to construct a patient-specific segmented model, we propose to fit the anatomically correct reference segmented model by patient anthropometric and CT/MRI data.

The first step is anthropometric scaling. The reference model can be split into several parts and adjusted by the height according to the height of the related parts of the actual patient. In the same way the width is adjusted. This scaling is not sufficient since the patient may have different body constitution: fat/muscle ratio, pathologies, anatomical features, etc.

On the second step we propose a transformation of the segmented reference model using control planes and control points. At first, several control planes are selected and patient CT/MRI image is fitted to the reference model image in these planes.

Model fitting in every plane is based on the piecewise affine mapping defined by the set of control points. The user marks the same set of control points both on the reference image and on the patient image. Then the reference image is mapped to the patient image shifting the control points from original positions to the new ones. The control points may represent anatomical or geometric features of the human body. We assume here that anatomical structure on the segmented images of the reference and patient models is the same. The size and the form of the contours (material boundaries) may be varied using this fitting.

The piecewise affine transformation is constructed on the basis of the Delaunay triangulation for the control points from the patient image. The same triangulation with the identical topology is constructed using the corresponding control points in the reference image. Assuming the latter triangulation is not tangled we can construct the piecewise affine mapping of each triangle from one mesh to the corresponding triangle in the second mesh. An example of the transformed segmented image is presented in Fig. 9.3.

Once the transformations on two parallel control planes are constructed we can define the transformation on any plane between these planes using linear combination of these two transformations.

To make the piecewise affine transformation isomorphic, we assume that both Delaunay meshes are not tangled. If the user specifies the positions of control points in such a way that the Delaunay mesh tangles, we propose to set auxiliary points. These points and the control points are used to construct a more flexible Delaunay mesh. Auxiliary points are placed between user defined control points in order to
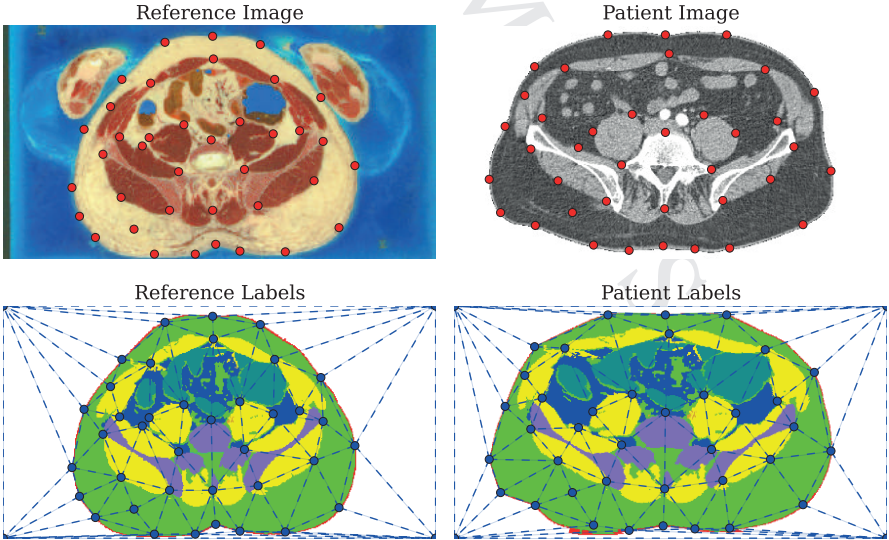

Fig. 9.3. Control points mapping. *Left:* the reference segmented image with control points. *Right:* the mapped image with control points

smooth the mesh deformation. The positions of the auxiliary points are determined by the variational mesh modification method. The detailed algorithm for such mesh adaptation is presented in [5]. The number of auxiliary points needed to create a set of untangled meshes may vary depending on the positions of control points. In practice, if the control points movements are small enough, we do not need any auxiliary points. If the deformation is not very large, the number of auxiliary points is also not too large.

Once the segmented patient-specific model is ready, one can apply already discussed *automated* tetrahedral meshing procedures.

The proposed technique is used to fit reference segmented model for patients with the same anatomical structure. This process relies on some expert-defined control points sets. Once the new automated control point detection algorithm is developed, this mapping technique may be extended automatically. Patients with different anatomical structure, i.e. with some pathologies, should be treated with other reference models.

9.4 Personalized Skeletonisation and Meshing of Network Structures

The algorithm of vessel graph reconstruction is divided into the following steps: 3D volume segmentation of vascular structure, meshing and centerlines extraction by VMTK, centerlines merging and graph reconstruction.

We should note that commercial software Amira® provides about the same functionality. It helps to perform semi-automatic blood vessels segmentation as well as to produce skeletonisation based on distance map and thinning methods providing connected set of voxels. After that Euclidean distance to the nearest boundary is calculated at every point to generate centerlines and spatial vascular graph.

In this work we propose a method which uses open source library VMTK. This library can be modified and easily extended with new methods. We use VMTK to produce centerlines of the 3D vascular domain extracted from CT/MRI data and extend it with the new algorithm for graph reconstruction. To perform vascular domain extraction, we filter input data and eliminate bones, void regions and surrounding tissues from the original image by thresholding. The level set method is used for tracking vascular branches and marching cubes method is used to extract the surface. The result of this preprocessing stage based on patient CT data is presented in Fig. 9.4.

The spatial vascular graph of the vascular network is described by a set of vertices A_i with radius vectors $\mathbf{a_i} = (x_i, y_i, z_i)$ and a set of edges given in terms of edge endpoints, length of the vessel segment and its averaged radius. This representation can be produced from centerline extraction of the initial 3D vascular domain. Several methods of centerline extraction are compared in [8, 16]. We select the method from VMTK based on Voronoi diagrams [2]. The result of meshing and centerlines computation is presented in Fig. 9.5.
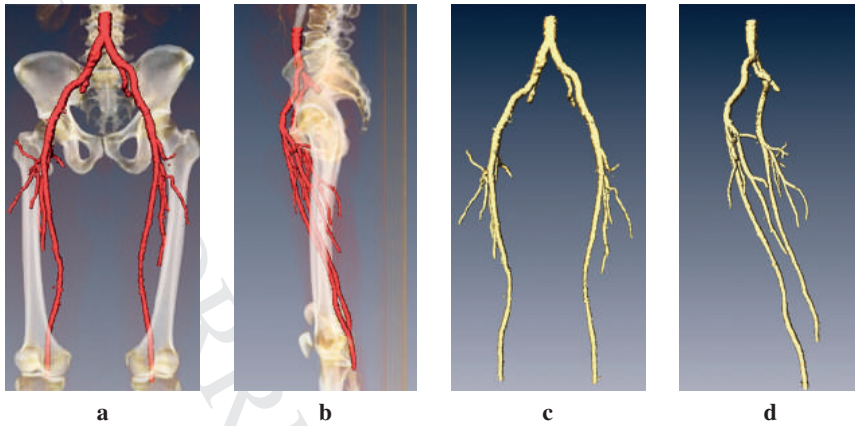
Fig. 9.4. 3D segmentation based on CT data: vessels with bones (a,b); vessels (c,d)
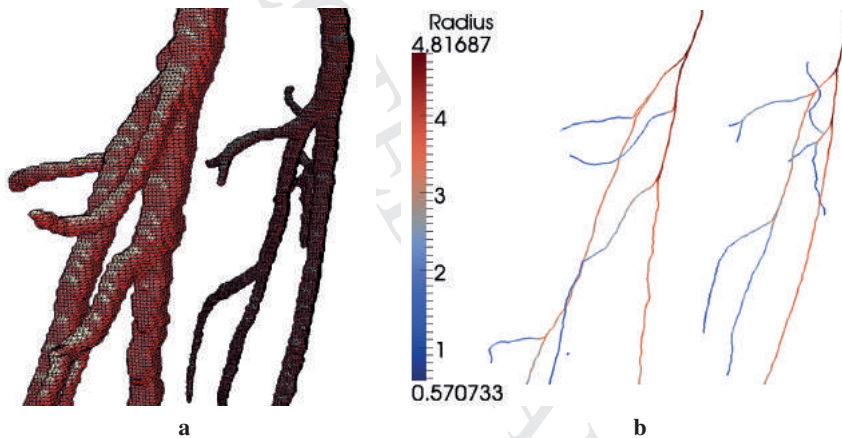

Fig. 9.5. 3D vascular domain: polygonal surface mesh (a); computed centerlines (b)

9.4.1 Skeletonisation Algorithm

Every centerline extracted with VMTK goes from every chosen inlet to every outlet. It is described by ordered set of pairs $(\mathbf{a}_i, r_i)$, where $\mathbf{a}_i = (x_i, y_i, z_i)$ is radius vector of the central point in the vessel cross section and r_i is the mean radius of the vessel at this point. These centerlines are merged by removing coincided parts and segmented with junction points. In Fig. 9.6 we demonstrate the set of centerlines $[O,P], [O,Q], [O,R], [O,S]$ before splitting and the new segmented set $[O,P], [O_1,Q]$, $[O_2,R], [O_3,S]$.

Centerlines intersection is determined by the following condition. Centerline $C' = \{(\mathbf{a}'_i, r'_i)\}_{i=1}^{n'}$ intersects centerline $C = \{(\mathbf{a}_i, r_i)\}_{i=1}^{n}$ if

$$\exists \mathbf{a} \in \{\mathbf{a}'_1, \ldots, \mathbf{a}'_{n'}\}, \ \exists k \in \{1, .., n-1\} : |\mathbf{a} - \mathbf{a}^*| \leq r_{k+0.5}(\mathbf{a}^*)$$
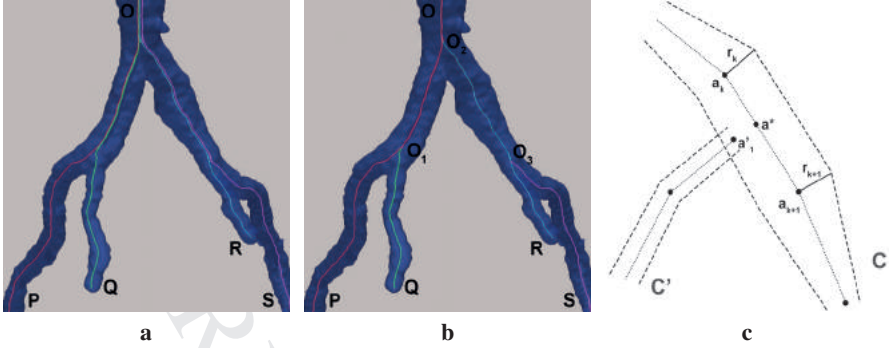
Fig. 9.6. Centerlines before (a) and after (b) splitting; intersection of centerlines (c)

where $\mathbf{a}^*$ is the projection of $\mathbf{a}$ onto $[\mathbf{a}_k, \mathbf{a}_{k+1}]$ and $r_{k+0.5}$ is obtained by the linear interpolation between the radii of two neighbours

$$r_{k+0.5}(\mathbf{a}^*) = \begin{cases} r_k(1 - \lambda_{k+0.5}(\mathbf{a}^*)) + r_{k+1}\lambda_{k+0.5}(\mathbf{a}^*), \mathbf{a}^* \in [\mathbf{a}_k, \mathbf{a}_{k+1}] \\ \qquad\qquad\qquad\qquad\qquad\qquad 0, \mathbf{a}^* \notin [\mathbf{a}_k, \mathbf{a}_{k+1}], \end{cases}$$

$$\lambda_{k+0.5}(\mathbf{a}^*) = \frac{|\mathbf{a}^* - \mathbf{a}_k|}{|\mathbf{a}_{k+1} - \mathbf{a}_k|}.$$

We define $\mathbf{a}^*$ as the branching point (Fig. 9.6c).

The algorithm of skeletonisation is initialized by choosing the root centerline. The other centerlines are checked for the intersection with the root; branching points are determined for every intersection. After that the algorithm recursively proceeds through the centerlines intersecting the root taking them subsequently as new roots. This can produce a graph with loops, but with vertices degree not greater than 3.

In order to avoid generation of branches with extra small length, we define the minimal branch length value $\Delta \in [2R(x), 4R(x)]$, where $R(x)$ is the local vessel radius at centerline point x. Then we merge points for centerline $C = \{(\mathbf{a}_i, r_i)\}_{i=1}^n$ as follows.

If

$$\exists \mathbf{a}_i, .., \mathbf{a}_{i+k} \in C : \sum_{j=0}^{k-1} |\mathbf{a}_{i+j+1} - \mathbf{a}_{i+j}| < \Delta,$$

and

$$\nexists \mathbf{a}_{i-1}, \mathbf{a}_{i+k+1} : |\mathbf{a}_i - \mathbf{a}_{i-1}| < \Delta, |\mathbf{a}_{i+k+1} - \mathbf{a}_{i+k}| < \Delta,$$

then redefine

$$\mathbf{a}_i = \cdots = \mathbf{a}_{i+k} = \sum_{j=0}^{k} \frac{\mathbf{a}_{i+j}}{k+1}.$$

The process is illustrated in Fig. 9.7 where only one vertex P_k is added to the set of graph nodes.

The complexity of the skeletonisation algorithm is $O\left(M^2 N\right)$ where M is the number of centerlines, N is the maximal number of points in the centerlines. The PC run
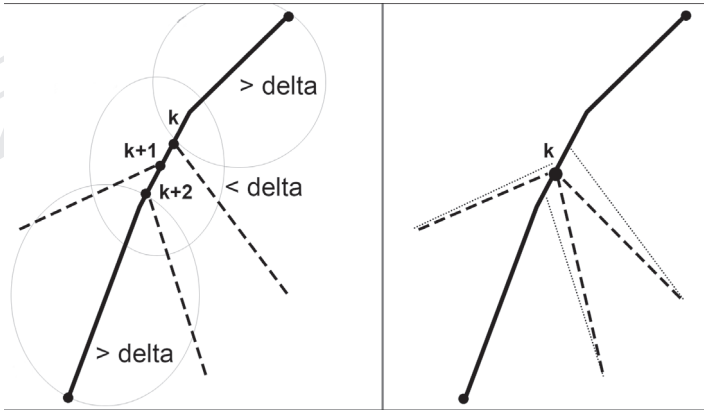
Fig. 9.7. Points merge due to the minimal branch length
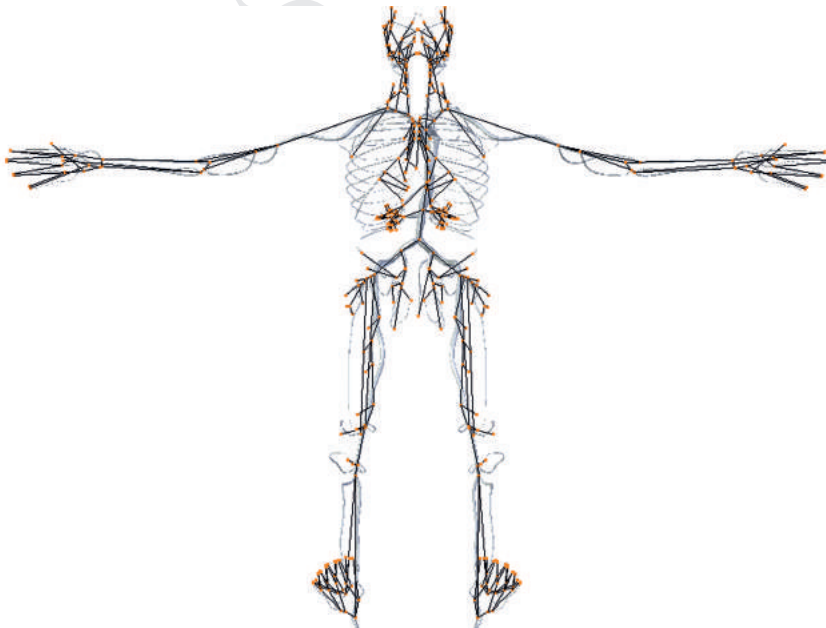

Fig. 9.8. The vascular network of arterial part of systemic circulation based on virtual 3D model [43]

time for the automated skeletonisation is of order of one minute in case of $M = 200$ and $N = 200$. The meshing procedure for the vascular graph is trivial since the mesh nodes are added uniformly on each graph edge.

The skeletonisation and meshing algorithm was tested on the vessel network given by the vascular 3D geometric model [43]. The resulting core graph for systemic arteries is presented in Fig. 9.8.

9.4.2 Application to Occlusion Treatment of the Femoral Artery

We consider the application of the hemodynamic model for thigh vasculature in the case of the occlusion treatment in femoral artery.

Presurgical patient specific CT data were used to produce vascular graph of the thigh arterial vasculature with the method discussed above. The arteries and resulting graph of vessels are presented in Fig. 9.4 and Fig. 9.9, respectively. The geometric parameters of the vascular network are identified by our skeletonisation algorithm and correspond to the patient specific morphology.

In this paper we omit the description of boundary conditions at the network inlet and outlet as well as the description of parameters c_k in (9.11) and the hydraulic resistances R_k^l in (9.9). Presurgical values of c_k and R_k^l are fitted to match the available presurgical Doppler ultrasound measurements at some points of the vascular network and general values provided by [3, 11, 22, 23]. These issues constitute the body of another paper [26]. Here we present only geometric parameters identified by the skeletonisation algorithm.

Table 9.1. Parameters of the arterial part: l_k is length of the kth vessel, d_k is diameter of the kth vessel, * denotes vessel without occlusion, ** denotes vessel with occlusion

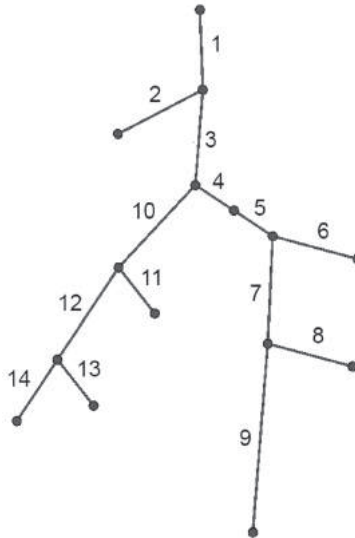| k	1	2	3	4	5*	5**	6	7	8	9	10	11	12	13	14
l_k, cm	4.63	6.51	14.09	1.0	0.79	0.79	4.11	2.08	8.07	38.75	1.67	4.5	8.17	3.55	12.7
d_k, cm	1.25	0.72	0.94	0.93	0.93	0.37	0.45	0.84	0.41	0.61	0.83	0.46	0.63	0.45	0.44

Fig. 9.9. Arterial network of the left thigh

The occlusion is modeled as a fragment of femoral artery (vessel 5 in Fig. 9.9). Except for vessel 5 we assume the model parameters l_k, d_k, c_k, R_k^l remain the same for the postsurgical case since the Reynolds number is not changed significantly in the most vessels in presurgical and postsurgical simulations. During presurgical simulations parameters of vessel 5 are modified as follows. The hydraulic resistance is increased by the factor 3, diameter is decreased by 60% thus providing lumen decrease (S_0 in (9.11)) by 84%. During postsurgical simulations parameters of vessel 5 were set equal to parameters of the normal femoral region 4 (Fig. 9.9).

We applied the personalized hemodynamic model to predict postsurgical blood flow through the left thigh arteries without occlusion. Measured peak velocities were used in this case to check the model output. The column *postsurgical* in Table 9.2 (for details see [26]) shows quite good coincidence between these data sets. The maximum relative error is not greater than 20% that is observed in distal part of superficial femoral artery. The maximal error is attributable to insufficient CT resolution. General anatomy [27] states that one of the deep femoral artery branches has a connection with the popliteal artery which provides an alternate pass in the case of femoral artery occlusion. We failed to observe this connection in patient CT data. Being introduced to the model, the alternate pass would decrease the peak velocity due to occurrence of the collateral flow and thus decrease the error.

Table 9.2. Peak blood velocities

| Measurement points (see Fig. 9.9) | Peak blood velocity (cm/s) | | | |
| | presurgical | | postsurgical | |
	patient	model	patient	model
3 - common femoral art.	148	149	150	155
4 - superficial femoral art. (proximal)	48	54	65	70
12 - deep femoral art.	103	93	69	83
5 – occlusion	above 300	340	–	71
7 - superficial femoral art. (distal)	–	67	98	86
9 - popliteal art.	52	56	72	72

9.5 Conclusions

In this work we addressed approaches for personalized anatomical meshing of the patient body or patient vascular network.

For patient-specific body meshing we adopt the four-stage algorithm which relies on the assumption that the patient has the same structural body composition as the reference VHP model, i.e. the same set of tissues and organs. First, we apply the semi-automatic segmentation of the reference VHP images. This is tedious work to be done only once. Second, we perform the anthropometric mapping of the reference model to the patient dimensions. Third, for selected cross section planes we generate the piecewise affine transformation to map the reference segmentation to the patient

segmentation on the basis of user-defined control points on both reference and patient images. The future development of the adaptation technique is expected to utilise either the automatic control points placement, or automatic mapping reconstruction techniques.

For patient-specific vascular network reconstruction we adopt the open source library VMTK to produce vascular centerlines on the basis of CT/MRI data followed by the automated skeletonisation algorithm. The produced vascular graph possesses all necessary geometric data for hemodynamic simulations. We demonstrated applicability of our approach to predictive personalized postsurgical blood flow simulations.

References

1. Abakumov, N.V., Mukhin, S.I., Favorski, A.P. et al.: Strategy of mathematical cardio-vascular system modeling. Matem. Mod.,**12**, 106–117 (2000)
2. Antiga L.: Patient-specific modeling of geometry and blood-flow in large arteries. PhD thesis. Politecnico di Milano, Milan (2003)
3. Caro, C.G., Pedley, T.J., Schroter, R.C., Seed, W.A.: The Mechanics of the circulation, Oxford University Press, Oxford, New York (1978)
4. Danilov, A.A.: Unstructured tetrahedral mesh generation technology. Comp. Math. and Math. Phys. **50**, 139–156 (2010)
5. Danilov, A.A., Kramarenko, V.K., Nikolaev, D.V., Yurova, A.S.: Personalized model adaptation for bioimpedance measurements optimization. Russ. J. Numer. Anal. Math. Modelling **28**, 459–470 (2013)
6. Danilov, A.A., Nikolaev, D.V., Rudnev, S.G., Salamatova, V.Yu., Vassilevski, Yu.V.: Modelling of bioimpedance measurements: unstructured mesh application to real human anatomy. Russ. J. Numer. Anal. Math. Modelling **27**, 431–440 (2012)
7. Danilov, A.A., Salamatova, V.Yu., Vassilevski, Yu.V.: Mesh generation and computational modeling techniques for bioimpedance measurements: an example using the VHP data. J. Phys.: Conf. Series (2012) doi: 10.1088/1742-6596/407/1/012004
8. Diedrich, K.T., Roberts, J.A., Schmidt, R.H., Parker, D.L.: Comparing performance of centerline algorithms for quantitative assessment of brain vascular anatomy. Anat. Rec. (Hoboken), **295**, 2179 (2012)
9. Frey, P., George, P.-L.: Mesh generation: application to finite elements. Hermes Science, Paris, Oxford (2000)
10. Formaggia, L., Quarteroni, A., Veneziani, A.: Cardiovascular mathematics:Modeling and simulation of the circulatory system, DE: Springer, Heidelberg (2009)

11. Ganz, V., Hlavova, A., Fronek, A., Linhart, J., Prerovsky, I.: Measurement of blood flow in the femoral artery in man at rest and during exercise by local thermodilution. Circulation **30**, 86–89 (1964)
12. Grimnes, S., Martinsen, O.G.: Bioimpedance and bioelectricity basics. Elsevier, Amsterdam (2008)
13. Höhne, K.H., Pflesser, B., Pommert, A., Riemer, M., Schubert, R., Schiemann, T., Tiede, U., Schumacher, U.: A realistic model of human structure from the Visible Human data. Meth. Inform. Med. **40**, 83–89 (2001)
14. Hunter, P., Coveney, P.V., de Bono, B., Diaz, V., Fenner, J., Frangi, A.F., Harris, P., Hose, R., Kohl, P., Lawford, P., McCormack, K., Mendes, M., Omholt, S., Quarteroni, A., Skr, J., Tegner, J., Thomas, S.R., Tollis,Tsamardinos, I., I., HGM van Beek, J., Viceconti, A vision and strategy for the virtual physiological human in 2010 and beyond, M.: Philosophical Transactions of the Royal Society A: Mathematical, Physical and Engineering Sciences **368**, 2595–2614 (2010)
15. Kholodov, Y.A., Kholodov, A.S., Simakov, S.S., et al.: Computational models on graphs for nonlinear hyperbolic and parabolic system of equations. Proc. III European Conf. Comp. Mech. 43 (2006)
16. Liu, J., Subramanian, K.: Accurate and robust centerline extraction from tubular structures in medical images. In: Advances in Information and Intelligent Systems, part 2, Vol. 251, Springer Berlin Heidelberg, 139–162 (2009)
17. Magomedov, K., Kholodov, A.: Grid-characteristic numerical methods. Nauka, Moscow (1988) (in Russian)
18. Müller, L.O., Parés, C., Toro, E.F.: Well-balanced high-order numerical schemes for one-dimensional blood flow in vessels with varying mechanical properties. J. Comp. Phys. **242** 53–85 (2013)
19. Mynard, J.P., Nithiarasu, P.: A 1D arterial blood flow model incorporating ventricular pressure, aortic valve and regional coronary flow using the locally conservative Galerkin (LCG) method. Comm. Num. Met. Eng. **24**, 367–417 (2008)
20. Pedley, T.J., Luo, X.Y.: Modelling Flow and Oscillations in Collapsible Tubes. Theoret. Comput. Fluid Dynamics **10**, 277–294 (1998)
21. Rineau, L., Yvinec, M.: A generic software design for Delaunay refinement meshing. Comp. Geom. Theory Appl. **38**, 100–110 (2007)
22. Sala, R., Rossel, C., Encinas, P., Lahiguera, P.: Continuum of pulse wave velocity from young elite athletes to uncontrolled older patients with resistant hypertension. J. Hypertens **28**, 19.216 (2010)
23. Schmidt, R.F., Thews, G.: Human Physiology, Springer-Verlag, Berlin, Heidelberg (1989)
24. Simakov, S.S., Kholodov, A.S.: Computational study of oxygen concentration in human blood under low frequency disturbances. Mat. Mod. Comp. Sim. **1**, 283–295 (2009)
25. Simakov, S.S., Gamilov, T.M., Soe, Y.N.: Computational study of blood flow in lower extremities under intense physical load. Russ. J. Numer. Anal. Math. Mod. **28**,485–504 (2013)
26. Simakov, S., Gamilov, T., Vassilevskii, Yu., Ivanov, Yu., Kopylov, P.: Patient specific haemodynamics modeling after occlusion treatment in leg. Math. Model. Nat. Phenom. **9**, 85–97 (2014)
27. Standring, S.: Gray's Anatomy: The Anatomical Basis of Clinical Practice, 40th ed., Elsevier, Churchill-Livingstone (2008)
28. Taubin, G.: A signal processing approach to fair surface design. In: Proc. of the 22nd Annual Conf. on Comp. Graphics and Interactive Techniques, 351–358. ACM, N.Y. (1995)

29. Vassilevski, Y.V., Danilov, A.A., Nikolaev, D.V., Rudnev, S.G., Salamatova, V.Y., Smirnov, A.V.: Finite-element analysis of bioimpedance measurements. Zh. Vych. Mat. Matem. Fiz. **52**, 733–745 (2012) (in Russian)
30. Vassilevski, Y.V., Simakov, S.S., Dobroserdova, T.K., Salamatova, V.Yu.: Numerical issues of modelling blood flow in networks of vessels with pathologies. Russ. J. Numer. Anal. Math. Mod. **26**, 605–622 (2011)
31. Vassilevski, Y.V., Simakov, S.S., Kapranov, S.A.: A multi-model approach to intra-venous filter optimization. Int. J. Numer. Meth. Biomed. Eng. **26**, 915–925 (2010)
32. Vassilevski, Y.V., Simakov, S.S., Salamatova, V.Yu., Ivanov, Yu.A., Dobroserdova, T.K.: Blood flow simulation in atherosclerotic vascular network using fiber-spring representation of diseased wall. Math. Model. Nat. Phenom. **6**, 333-349 (2011)
33. Vassilevski, Y.V., Simakov, S.S., Salamatova, V.Yu., Ivanov, Yu.A., Dobroserdova, T.K.: Vessel wall models for simulation of atherosclerotic vascular networks. Math. Model. Nat. Phenom. **6**, 82-99 (2011)
34. Vassilevski, Y.V., Vershinin, A.V., Danilov, A.A., Plenkin, A.V.: Tetrahedral Mesh Generation in Domains Defined in CAD Systems. In: Matrix methods and technology for solving large problems, pp. 21–32. Inst. Num. Math., Moscow (2005) (in Russian)
35. Wilkinson, I.B., Cockcroft, J.R., Webb, D.J.: Pulse wave analysis and arterial stiffness. J. Cardiovasc. Pharmacol. **32** Suppl.3, S33–7(1998)
36. Wu, Z., Sullivan, J.M.: Multiple material marching cubes algorithm. Int. J. Numer. Meth. Eng. **58**, 189–207 (2003)
37. Xiao, N., Humphrey, J.D., Figueroa, C.A.: Multi-scale computational model of three-dimensional hemodynamics within a deformable full-body arterial network. J. Comp. Phys. **244**, 22–40 (2013)
38. Yushkevich, P.A., Piven, J., Hazlett, H.C., Smith, R.G., Ho, S., Gee, J.C., Gerig, G.: User-guided 3D active contour segmentation of anatomical structures: significantly improved efficiency and reliability. Neuroimage **31**, 1116–1128 (2006)
39. Advanced Numerical Instruments 3D http://sourceforge.net/projects/ani3d
40. The National Library of Medicine's Visible Human Project, http://www.nlm.nih.gov/research/visible
41. http://www.vmtk.org
42. http://www.amira.com, http://www.vsg3d.com/amira
43. Anatomy 3D Models – Placticboy. http://www.plasticboy.co.uk
44. http://www.inm.ras.ru/research/bioimpedance